TÜBİTAK

Turkish Journal of Earth Sciences

Volume 33 | Number 2 Article 6

1-29-2024

# DInSAR analysis and geophysical modeling of 2022 November 23 Gölyaka-Düzce Earthquake

ŞÜKRÜ ONUR KARACA
onurkaraca87@hotmail.com

GÜLTEKİN ERTEN
gultekinerten@hotmail.com.tr

BATUĞHAN YIKMAZ
batughanyikmaz@gmail.com

SELİM ÖZALP
selim.ozalp@mta.gov.tr



## Recommended Citation

KARACA, ŞÜKRÜ ONUR; ERTEN, GÜLTEKİN; YIKMAZ, BATUĞHAN; and ÖZALP, SELİM (2024) "DInSAR analysis and geophysical modeling of 2022 November 23 Gölyaka-Düzce Earthquake," *Turkish Journal of Earth Sciences*: Vol. 33: No. 2, Article 6. https://doi.org/10.55730/1300-0985.1906
Available at: https://journals.tubitak.gov.tr/earth/vol33/iss2/6

Turkish Journal of Earth Sciences

http://journals.tubitak.gov.tr/earth/

Research Article

Turkish J Earth Sci
(2024) 33: 192-207

doi:10.55730/1300-0985.1906

# DInSAR analysis and geophysical modeling of November 23, 2022 Gölyaka-Düzce Earthquake

**Şükrü Onur KARACA[1,*], Gültekin ERTEN[1], Batuğhan YIKMAZ[2], Selim ÖZALP[1]**

[1]Department of Geological Research, General Directorate of Mineral Research and Exploration, Ankara, Turkiye

[2]Department of Mining and Drilling, Turkish Petroleum International Corporation, Ankara, Turkiye

**Received:** 27.03.2023 • **Accepted/Published Online:** 12.11.2023 • **Final Version:** 29.01.2024

**Abstract:** Numerous significant earthquakes have occurred along the North Anatolian Fault Zone (NAFZ), Türkiye's most important fault zone. An earthquake with magnitude of Mw 6.0 occurred near the Gölyaka District of Düzce Province at 04:08 local time on November 23, 2022. According to the moment tensor solutions published by national and international seismology centers, the earthquake occurred at the northeast end of the Karadere segment within the NAFZ and was caused by a right-lateral strike-slip fault in the NW-SE direction. In this study, the differential interferometric synthetic aperture radar (InSAR) method was employed to analyze the deformation. Four Sentinel-1A complex datasets were used, two of which were ascending (2022/11/15 and 2022/11/27) and two of which were descending (2022/11/14 and 2022/11/26) pre- and postearthquake, to determine the deformation that occurred after the earthquake. In addition, surface deformation movements in both the east-west and vertical directions were calculated using these two data sets. Elastic dislocation modeling was performed by applying linear and nonlinear inversion to determine slip distribution related to the fault structure, using the displacement amount obtained from DInSAR results and data obtained from the Global Centroid Moment Tensor (GCMT) catalog. Based on the findings from the DInSAR analysis, subsidence of approximately 5 cm and eastward movement of 8 cm were detected on the northern block of the Düzce segment. This right-lateral movement corresponds to an area of approximately 105 km$^2$ northwest of the Düzce segment. On the southern block of the Düzce segment, elevation of about 3 cm and westward movement of about 3 cm were observed. Elastic dislocation modeling shows that the observed deformation model can be explained by slip on a single planar fault for the Gölyaka-Düzce earthquake. A right-lateral strike-slip fault with northwest dip was observed, extending down to a slip-centroid depth approximately 9.2 km within the upper crust region. The elastic slip modeling in this half-space resulted in a slip of 0.35 m, Mw of 6.1, strike of 264°, dip of 66°, and rake of –165°. This study reveals that the Düzce segment was the location where the earthquake occurred, but it is also believed that the Karadere segment was impacted by this seismic event. Overall, the study provides information about the occurrence of the Gölyaka-Düzce earthquake, subsequent deformation, and the elastic fault model in half-space.

**Key words:** Gölyaka-Düzce, DInSAR, earthquake, elastic model, Karadere Segment

## 1. Introduction

The Gölyaka-Düzce earthquake occurred approximately 16 km west of Düzce city, along the northern branch of the North Anatolian Fault System (NAFS), with right-lateral strike-slip motion on November 23, 2022 (Figure 1) (AFAD, 2022). From 04:08 GMT on November 23, 2022, to 08:00 GMT on November 25, 2022, a total of 220 aftershocks occurred in the region, two of which were larger than magnitude 4 (KOERI). In preliminary studies after the earthquake, Özalp et al. (2023) reported that no surface rupture was observed associated with the fault that caused the earthquake, but earthquake-related surface deformations of lateral spreading type were observed on the alluvial plain deposits where the Karadere segment intersects with the Büyük Melen River. Sözbilir et al. (2023) determined the earthquake to be 6.1 Mw with a south-dipping strike-slip motion in their tensor solutions.

In this investigation, we conducted an assessment of the tectonic features within the Düzce basin along the North Anatolian Fault (NAF), as well as an analysis of the surface deformations that occurred subsequently to the Gölyaka-Düzce earthquake of November 23, 2022, through the utilization of interferometric synthetic aperture radar (InSAR) and elastic modeling techniques. The moment tensor solution for the earthquake was calculated with data provided by AFAD[1].

1 AFAD (2022). Türkiye Cumhuriyeti İçişleri Bakanlığı Afet ve Acil Durum Yönetimi Başkanlığı [Online]. Website: https://deprem.afad.gov.tr/event-catalog [accessed 2023/01/11].

* Correspondence: onurkaraca87@hotmail.com

The InSAR method is widely used in active tectonic studies for determining surface subsidence resulting from earthquakes, volcanic eruptions, and landslides due to its ability to work in various time and weather conditions, wide spatial coverage, and high measurement accuracy (Bamler and Hartl, 1998). Examples of these studies include the mapping of surface deformations caused by the November 12, 1999, Düzce earthquake and determination of its fault geometry using InSAR by Çakır et al. (2003a). They also used elastic modeling with GPS and InSAR data to suggest that a probable Düzce earthquake could be multisegmented, and that an old thrust plane inclined to the north may rupture along with the vertical Düzce segment (Çakır et al., 2003a). In another study, Çakır et al. (2003b) calculated a model for the slip associated with the 1999 İzmit earthquake affecting the NAF at the eastern end of the Marmara Sea by combining tectonic field observations and SAR data. They described the main features of coseismic and postseismic deformation captured together in SAR data (Çakır et al., 2003b).

The February 6, 2017, Ayvacık-Çanakkale earthquake (Mw 5.3) was analyzed using the differential synthetic aperture radar (DInSAR) technique, and as a result, approximately 9 cm vertical displacement was detected in these areas (Abdikan et al., 2019). Another study of the February 2017 Gulpinar earthquake sequence (Biga Peninsula, Türkiye) illustrated four events with moment magnitudes $5.0 \leq Mw \leq 5.2$ on InSAR interferograms (Sentinel-1 satellites) to identify the seismic fault and seismological data and use this to refine geometry and kinematics using inversion techniques (Ganas et al., 2018). Tatar et al. (2020) mapped the surface rupture geometry with geomorphic structures in detail and associated them with satellite imagery and ground data in their study of the January 24, 2020, Elazığ-Sivrice earthquake. According to the results, InSAR studies showed 10 cm uplift of the northwestern block of the fault and 6 cm subsidence in the southeastern block (Tatar et al., 2020). Due to the difference in vertical movement between the two blocks of the fault, it was interpreted that a section of at least 30 km in length broke during the main shock on the Pütürge segment between southwest Sivrice and Pütürge (Tatar et al., 2020). Another study claimed that the 2020 Elazığ earthquake occurred on a steep, NW-dipping strike-slip fault (72 degrees) with 35 km rupture length (Melgar et al., 2020). Karaca and Erten (2023) used DInSAR and an elastic dislocation model to show surface deformation (rupture length 34.78 km) and fault parameters with slip ratio 1.95 m, Mw 6.75, focal depth 10 km, width 7.4 km, strike 240.27°, slope 69.19°, and rake 0.19°. For the same earthquake, Pousse Beltran et al. (2020) used InSAR and elastic modeling to state that the main shock of the earthquake spread mostly westward with 10° fault dip-direction angle from the focal point. They noted that the rupture occurred only at one end of the DAF segment boundary and that the 1874-M ~ 7.1 Gölcük Lake earthquake had spread to the slip area (Pousse Beltran et al., 2020). Another investigation revealed the properties of the seismic fault, including its location, geometry, and geodetic moment. These investigations focused on a notable Mw = 7.0 earthquake that took place on October 30, 2020, in the northern area of Samos, Greece. They showed the impact of the earthquake with various effects such as liquefaction, rock falls, rock slides, road cracks, and extensive landslides (Ganas et al., 2021).

The way to explain InSAR data and tectonic observations is to determine the parameters of faulting in deformation zones resulting from the earthquake using elastic modeling. In this study, attempts were made to identify the direction angle, dip angle, strike vector, and shear amount with values such as the fault's basic geometry using the elastic modeling method. Although there are many studies about elastic displacement theory in space (Stekeete, 1958; Press, 1965; Wright et al., 1999), Okada's (1985) studies constitute the most general theory. These studies are based on a formulation that allows effective analytical calculation of the sliding area that is caused by the displacement occurring on a rectangular or triangular surface area in a spatial environment. Using this formulation, the displacement amount that occurs on the earth's surface as a result of any fault movement described by the earthquake source parameters can be calculated. Many researchers have conducted various studies about both the application of this theory to the Earth's crust and its application with interferometry (Wells and Coppersmith, 1994; Wright et al., 1999; Çakır et al., 2003b; Wang et al., 2004; Funning et al., 2005; Liu, 2015; Tiryakioğlu et al., 2018; Pousse Beltran et al., 2020).

## 2. Materials and methods

### 2.1. Study area

The study area covers the regions between the latitudes of 40°47′N and 41°00'N and the longitudes of 30°45′E and 31°25′E, including the settlements of Gölyaka and Gümüşova from southwest to northwest, and the area where the city center of Düzce is located in the east (Figure 1A).

Tectonically, the most important feature in the region is the NAF. The NAF, which caused many casualties and property damage in 1999, generated the 7.4 Mw İzmit and 7.2 Mw Düzce earthquakes in the same year. These two earthquakes, which were caused by adjacent fault segments, created a surface rupture of about 200 km long along the North Anatolia Fault Zone (NAFZ) (Çakır et al., 2003b). This earthquake, which caused massive destruction, occurred on the Akyazı-Gölyaka-Düzce

segment. This segment separates the Western Pontides zone from the Armutlu-Almacık-Arkotdağ zone (Gedik and Aksay, 2002). In a study conducted by Yıldırım and Tüysüz (2017) about the Almacık block located south of the study area, it was observed that the Almacık Block, associated with the NAFZ, moved in a clockwise direction by 20° ± 2°. This clockwise rotation was completed in geological time.

The study area is generally cut by east-west trending faults, and the Düzce segment, which extends from the western to the eastern boundary in the south, is a 40-km-long east trending right-lateral strike-slip fault. This segment, which is the focal point of the study, intersects with the Karadere segment, a 33.- km-long N71°E right-lateral strike-slip fault, to the west (Figure 1A). Further to the north, the Hendek Fault (N75°E right-lateral strike-slip fault) and Çilimli Fault (N70°E 35°-40° NW dipping reverse fault) form the northern boundary (Emre et al., 2013). The location of the study area in Türkiye and the stations obtained from AFAD for the moment tensor solution are shown in Figure 1B.

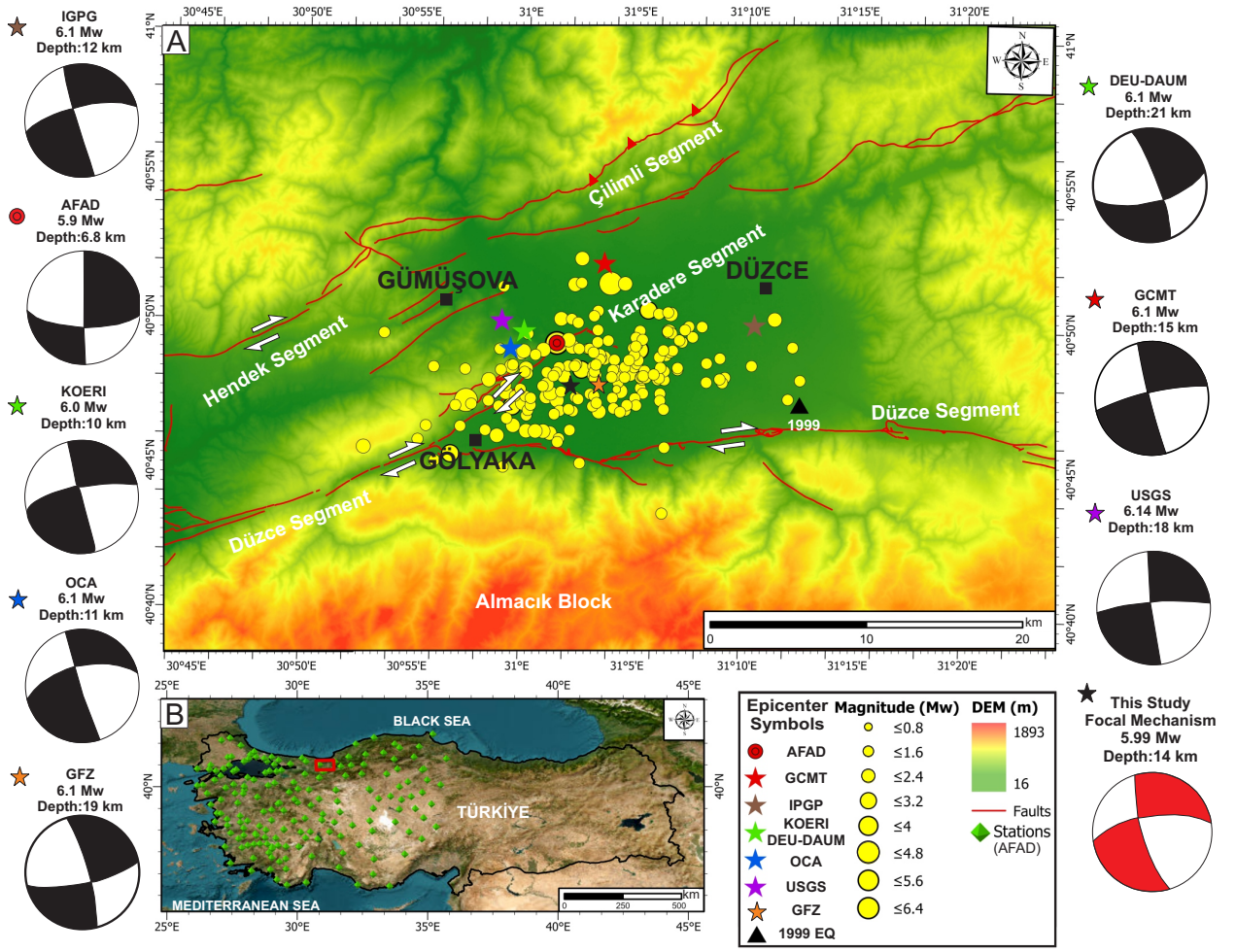


**Figure 1.** A) The digital elevation model of the Gölyaka-Düzce region. Yellow dots represent earthquakes in the range of 0.1–6.4 Mw between 22/11/2022 00:01 and 24/11/2022 23:59, taken from AFAD[1]. Colored stars show the center points of the Düzce-Gölyaka earthquake of 23 November 2022, which are indicated according to different observation stations. The black triangle shows the earthquake center of the 1999 Düzce earthquake according to AFAD. Focal mechanism solutions are modified from the European-Mediterranean Seismological Center (EMSC[1], 2022). Active faults are shown with red lines in the Turkey Active Fault Map (Emre et al., 2013) published by MTA. B) The location of the study area in Türkiye is shown with red rectangles. The green diamond shapes show the earthquake stations taken from AFAD for the moment tensor solution.

**2.2. DInSAR method**

DInSAR is a remote sensing method that can reveal surface deformations on the earth with cm-level precision and wide coverage area (Zebker and Goldstein, 1986). SAR systems represent images as complex numbers (Zebker and Goldstein, 1986). Attempts are made to identify deformations on the earth's surface caused by natural events such as earthquakes using the pre- and postdeformation phase differences on the SAR images consisting of complex numbers (Yague Martinez et al., 2016). With the InSAR technique, a new image is obtained by calculating the phase differences of corresponding pixels between two synthetic aperture radar images of the same region, and this new image is called an interferogram (Helz, 2005). The interferogram provides information about the height of the target area as well as small changes in the range distance between the two images (Yague Martinez et al., 2016). Small changes in range distance create fringe interference patterns due to phase differences, and these structures can be used to measure topography and surface deformations with the InSAR technique (Sarychikhina and Glowacka, 2015). Each cycle of the phase in the fringe structure corresponds to half the wavelength of changes in the satellite-earth distance (Çakır et al., 2003b; Torres et al., 2012).

With two separate interferograms as a master and slave images, deformation information is obtained. These interferograms are referred to with the formula below (Yague-Martinez et al., 2016) ;

$$\Delta\phi_{int} = \Delta\phi_{deformation} + \Delta\phi_{topo} + \Delta\phi_{orbit} + \Delta\phi_{atm} + \Delta\phi_{noise} \quad [1]$$

In the equation, the phase difference is referred to as $\Delta\phi_{int}$, surface deformation as $\Delta\phi_{deformation}$, the effect of surface topography as $\Delta\phi_{topo}$ , residual phase occurring due to orbit error as $\Delta\phi_{orbit}$, atmospheric noises of humidity, heat and pressure as $\Delta\phi_{atm}$, and random noises caused by unknown effects as $\Delta\phi_{noise}$. . The purpose of DInSAR studies is to try to find $\Delta\phi_{deformation}$ by using the phase difference between two radar images ($\Delta\phi_{int}$). In this study, four Sentinel 1A complex data sets provided by the European Space Agency (ESA), two of which are ascending (dated 2022/11/15 and 2020/11/27) and two are descending (dated 2022/11/14 and 2020/11/26), were processed using Envi 5.6.2 software for both pre- and postearthquake periods (Table 1). The steps used for DInSAR data processing are shown in Figure 2A.

Satellite radar interferometry (InSAR) is a powerful technique for monitoring deformation phenomena. While deformation phenomena occur in a three-dimensional (3D) world, one of the limitations of InSAR phase observations is that they are only sensitive to the projection of the 3D displacement vector onto the radar line-of-sight (LoS) direction. The following equations are used to separate the LoS displacement estimates from the ASC and DESC orbitals into EastWest [2] and UpDown [3] components (Kotulak et. al., 2022).

$$Disp_{EW} = \frac{cos\theta_D Disp_A - cos\theta_A Disp_D}{cos\theta_A sin\theta_D cos_{\alpha_D} - cos\theta_D sin\theta_A cos_{\alpha_A}} \quad [2]$$

$$Disp_{UD} = \frac{sin\theta_D cos_{\alpha_D} Disp_A - sin\theta_A cos_{\alpha_A} Disp_D}{cos\theta_A sin\theta_D cos_{\alpha_D} - cos\theta_D sin\theta_A cos_{\alpha_A}} \quad [3]$$

In this context, $\alpha_A$ represents the azimuth angles of ascending orbits, while $\alpha_D$ indicates the azimuth angles of descending orbits. $\theta_A$ signifies the look angles in ascending orbits, whereas $\theta_D$ represents the look angles in descending orbits. Additionally, $Disp_A$ corresponds to the displacement on the ascending LoS, and $Disp_D$ shows the displacement on the descending LoS.

**2.3. Elastic dislocation modeling**

Earthquakes that cause significant changes in surface deformation are generally expected to have a seismic moment magnitude (Mw) greater than 6.0 (Aktuğ, 2003). Surface changes were calculated using DInSAR data before and after the November 23, 2022, Gölyaka-Düzce earthquake, and the slip (lateral and vertical displacement) amounts, length, width, depth, strike, slope, and other geometry parameters of the fault planes were calculated using tensor solution parameters from the Global Centroid-Moment-Tensor (CMT) catalog. ENVI-SarScape 5.6.2 software was used for modeling studies. The data processing steps are shown in Figure 2B.

The first data processing step in elastic dislocation modeling includes area selection and image sampling. Image sampling is necessary to reduce the number of points to be modeled and ascending data processing speed. The Quadtree algorithm, a data reduction algorithm, was used to sparsely sample the image range without causing signal loss (Welstead, 1999). Using InSAR values, the lateral and vertical displacement amounts, length, width, depth, strike, slope, and other geometric parameters of the fault planes that cause deformation on the Earth's surface are calculated from the sparsely sampled image, and this process is performed using linear and nonlinear inversion (Sarmap[2]).

Before explaining linear and nonlinear inversions, the concept of inversion must be explained. The concept of inversion is defined as the calculation of the parameter

2 Sarmap (2018). ENVI SarScape v5.5.0: Geophysical Modeling Tutorial [Online]. Website: https://www.sarmap.ch/tutorials/GeophysicalModelingTutorial_55.pdf [accessed 2022/02/03].

values of a conceptual model using the measured data (Başokur, 2015). In other words, the differences between the measured data and the theoretical data must be calculated to provide objective reality for any proposed model. One of the methods used to produce various models for inversion is the derivative-based method. In this study, a derivative-based inversion process was also used. In the derivative-based inversion processes, if the relationship between data and parameters is defined by a string equation, it is called linear inversion. If the relationship between data and parameters cannot be expressed by string equations, it is called nonlinear inversion. The inversion process is applied to obtain the displacement or displacement distribution on a volcanic vent, a dike, or a fault in elastic dislocation modeling. Firstly, a nonlinear inversion process is carried out. Nonlinear inversion, is used to find the most suitable source parameters to minimize a cost function based on the difference between observed and predicted geodetic data. Multiple iterative processes are carried out to increase the probability of the cost function approaching the global minimum function. The method applied for this process is based on the Levemberg-Marquardt algorithm (Marquardt, 1963). The Levemberg-Marquardt minimization algorithm possesses a similar characteristic to gradient methods in that it can converge even when starting from an initial guess outside the convergence region of other methods. Additionally, like the Taylor series method, it can quickly approach the converged values once it enters the vicinity. As a result, this method combines the favorable aspects of its predecessors while bypassing their major limitations (Marquardt, 1963). The determination of the underground structure is ensured by starting from a certain initial model and using the possible appropriate parameters until conformity between the observational anomalies and the theoretical anomalies created by the model reaches the optimum level (Aşcı and Yas, 2017). In the next stage, the aim is to obtain the slip distribution on the fault plane by using the linear inversion process. In the linear inversion process, the parameters of the structure are directly determined (Aşcı and Yas, 2017). When the relevant geometry and slip parameters for the fault plane and the earthquake are known, the process of calculating the effects of the earthquake moment on the input data used in the initial data processing, which is called forward modeling, is performed using the elastic models for the earthquake. The steps used in data processing for elastic dislocation modeling are shown in Figure 2B.

In addition, Monte Carlo analysis was applied in this study to verify the accuracy of earthquake parameters. Monte Carlo analysis is a numerical method of simulating an event and is based on probability theory. This methodology utilizes statistical sampling and random simulations to estimate uncertainties and evaluate the accuracy and dependability of InSAR measurements and derived parameters (Parsons et al., 2006). When applied to a numerical inversion problem, it relies on generating random numerical values and repeated simulations to approximate the parameter of interest based on the simulation results.

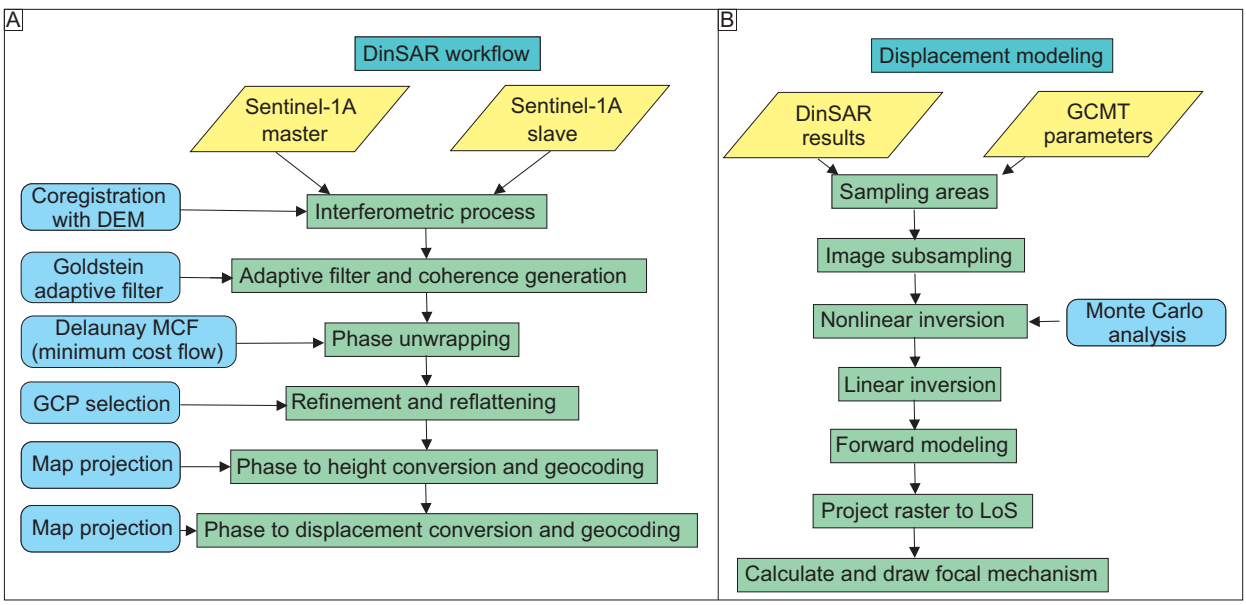


**Figure 2.** A) DInSAR data processing flow. B) Data processing flow used in elastic dislocation modeling.

**2.4. Moment tensor analysis**

Many methods were developed based on the motion and propagation direction of seismic waves emitted during an earthquake to calculate the focal mechanisms of earthquakes. The moment tensor analysis method allows the seismic source causing the earthquake to be represented by a tensor consisting of force couples (Stein and Wysession, 2003). This method allows the calculation of fault parameters by inversion of observational seismograms. Faulting, the earthquake source, is also represented by the body forces of wave propagation. Displacement at any point on the Earth's surface can be expressed as a linear combination of time-dependent moment tensor elements (Jost and Hermann, 1989).

There are some specific features of seismic waves propagating throughout the Earth's crust following an earthquake. First, the mass forces associated with the earthquake source do not spread over a volume but rather along a fault. Second, the earthquake source is represented not only by single forces but also by dipole forces. Dipole forces cause the mutual movement of two blocks on either side of the fault (Figure 3A). These are defined along the Σ fault by the moment tensor density (Figure 3B).

The moment tensor M is a symmetric tensor that defines nine pairs of equivalent dipole forces that can move in the earthquake source. The components of the moment tensor are defined by the scalar moment Mo, the direction (ϕ), dip (δ), and shear displacement (λ).

**2.4.1. Moment tensor analysis of the Düzce earthquake**

The waveform data required for tensor analysis of the Düzce earthquake was provided by Earthquake Data Center System of Türkiye (TDVMS). Broadband velocity stations with a diameter of approximately 350 km were used for waveform data. The hypocenter parameters (location, depth, and occurrence time) of the earthquake were obtained from Kandilli Observatory and Earthquake Research Institute (KOERI).

The calculated (red) and synthetic (blue) waveforms obtained after the inversion are shown in Figure 4A with the three components plotted at the same scale. The

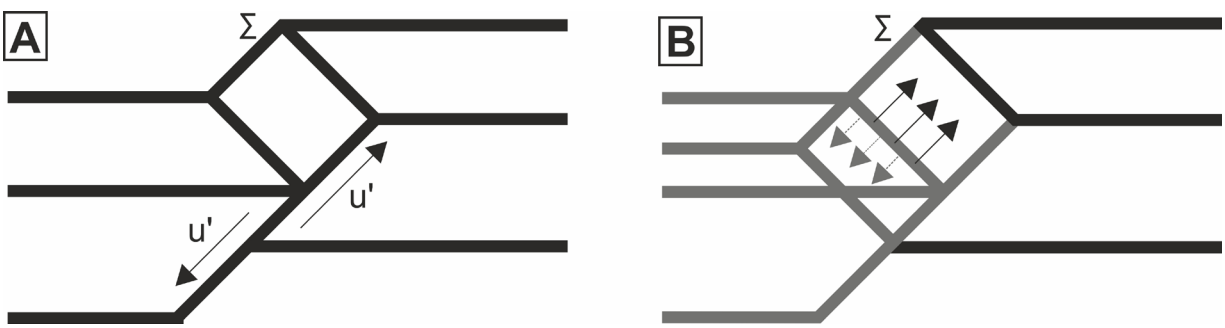


**Figure 3.** A) Normal fault motion pattern and B) Σ represent equal distribution of dipole forces along the fault (Vavryčuk, 2015).

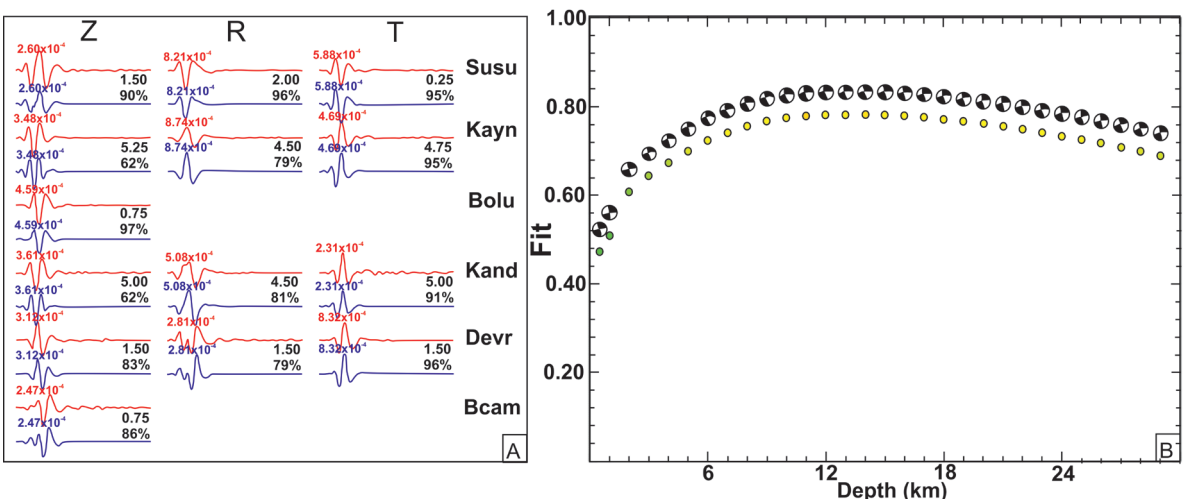


**Figure 4.** A) Depth sensitivity for the waveform mechanism. It shows the best depth match. B) Synthetic and calculated waveforms for each component as a result of inversion.

number in the top right of the synthetic trace represents the time shift required for maximum correlation between the calculated and synthetic traces. The number at the bottom represents the percentage reduction in variance (variation) for each trace (100% indicates perfect fit). Figure 4B shows the depth sensitivity graph for the best depth match to the waveform mechanism. The fault kinematic parameters obtained from the waveforms calculated after the inversion are shown in Table 2.

## 3. Results

### 3.1. DInSAR results

Fringe structures related to the surface deformation that occurred after the earthquake can be seen in the phase map generated from DInSAR results (Figures 5A and 5B). After unwrapping the phase differences of these fringe structures, the surface deformation that occurred after the Gölyaka-Düzce earthquake on November 23, 2022, is shown (Figures 5C and 5D). The surface deformation after the earthquake is interpreted in the LOS direction. Here, positive values indicate movement approaching toward the satellite in the LOS direction, and negative values indicate movement away from the satellite in the LOS direction. Accordingly, in the ascending data set, maximum –7.2 cm movement away from the satellite towards the northeast direction of the Karadere segment can be interpreted as movement to the east or subsidence. When the ascending and descending data sets are separated into components, the east-west and uplift-subsidence movements can be obtained. In the east-west direction, positive values indicate eastward movement, and negative values indicate westward movement. Positive values of approximately 6–8 cm in the northwestern part of the earthquake epicenter and the northern block of the Karadere segment are seen as eastward movement (Figure 5E). In Figure 5F, positive values indicate upward movement, and negative values indicate subsidence. In contrast, a subsidence movement of about –5 cm was observed in the northwestern part of the Karadere segment.

### 3.2. Elastic dislocation modeling results

The displacements obtained from DInSAR data and earthquake information obtained from GCMT were modeled in the half-space using elastic shear modeling to understand the fault mechanism and estimate earthquake source parameters. Monte Carlo analysis was used to determine the statistical mean intervals of the results obtained from nonlinear inversion.

Figures 6A and 6D depict the surface deformation observed through DInSAR, while Figures 6B and 6E illustrate the models generated through the nonlinear inversion process, based on Figures 6A and 6D. Figures 6C and 6F display the residuals and corresponding root mean square (RMS) values calculated from the shear dislocation. These residuals exhibit lower RMS values compared to the previous results, indicating that the corrected solution reduced the error rate.

The nonlinear inversion statistics showing the uncertainties and variations in the model parameters for the fault are given in Figure 7. In this figure, each of the 50 points represents the extent of variation for the optimal inversion solution associated with statistically different set of parameters (length, width, depth, dip, location information, strike, and slip amount). Red dots show the best value in the iteration process. The proximity of the other points to the best value and the shape of the clusters they form provides information about the accuracy of the model.

The slip amount that occurred during the November 23, 2022, Gölyaka-Düzce earthquake and the earthquakes that occurred between November 22, 2022, 00:01 and November 24, 2022, 23:59, ranging from 0.8 to 6.4 Mw, was expressed in 3D on the ascending data set (Figure 8A). Earthquake catalog data obtained from KOERI[3] and AFAD[1] are also shown with their coordinates, depth, and magnitude values. The modeled fault plane, which is interpreted as having 0.35 m of right-lateral and dip-slip rate below the topography, is shown in 3D, and the aerial view of the corresponding region is given in Figure 8B. Figures 8C and 8D depict the profiles represented by

3 KOERI (2022). Kandilli Observatory And Earthquake Research Institute. [Online]. Website: http://www.koeri.boun.edu.tr/sismo/zeqdb [accessed 2023/01/11].

**Table 1**. Characteristics of Sentinel-1 InSAR pairs ($B_\tau$: perpendicular baseline, $B_{ll}$: temporal baseline, Wl: wavelength, Pol: polarization).

| *Product type* | *Date* | *Mode* | *Pass* | *Pol.* | *Line-of-sight ıncidence angle, θ* | *line-of-sight azimut, α* | *$B_\tau$- Baseline perp $B_{ll}$- Baseline parallel* | *Band / Wl (cm)* | *Path* | *Frame No.* |
|---|---|---|---|---|---|---|---|---|---|---|
| *S1-A* | 2022/11/15<br>2022/11/27 | IW | Asc. | VV | ~38.04° | 80.1° | 92.6 (m) / 12 days | C/5.6 | 160 | 132 |
| *S1-A* | 2022/11/14<br>2022/11/26 | IW | Des. | VV | ~32.24° | 283.5° | 225.13 (m) /12 days | C/5.6 | 138 | 458 |

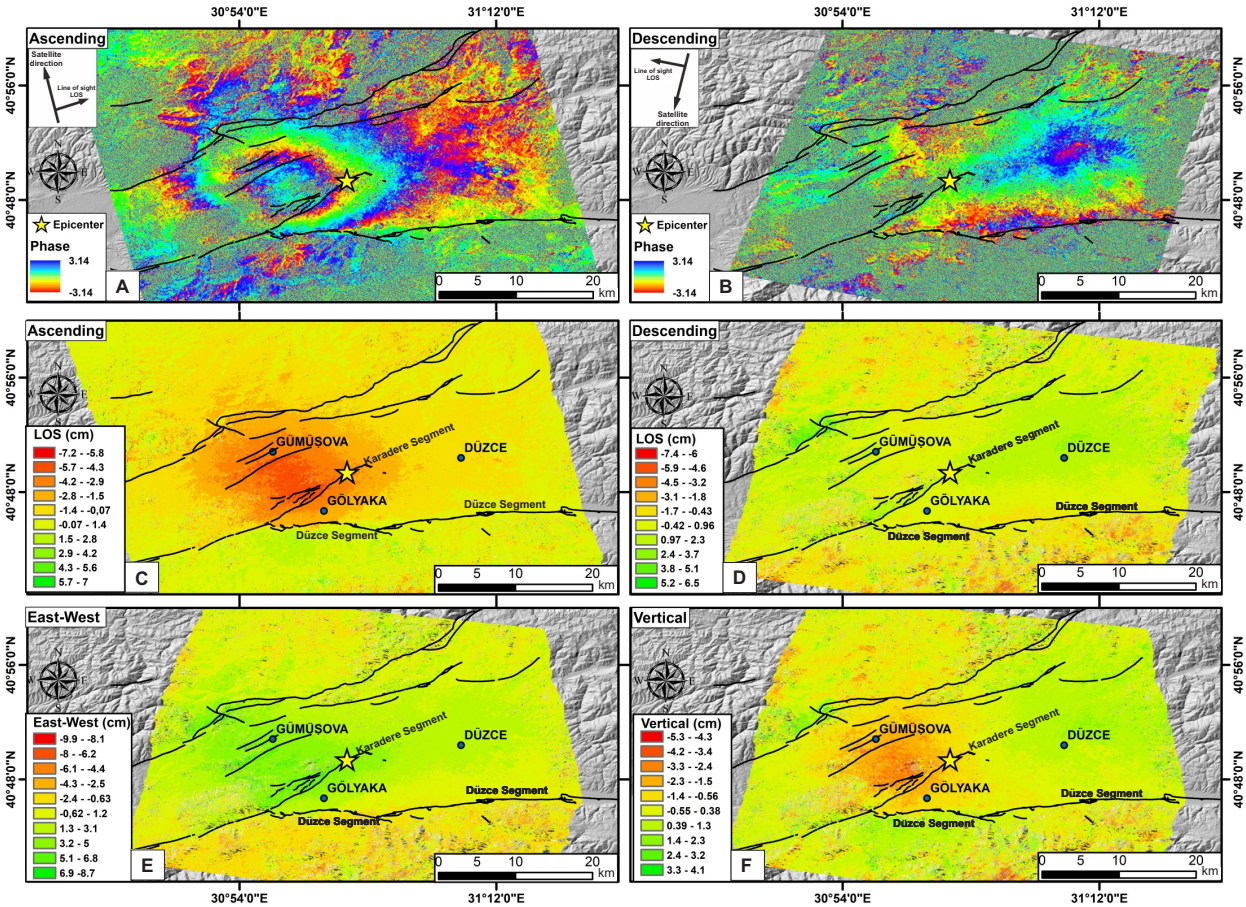


**Figure 5.** 23 November 2022 Gölyaka-Düzce earthquake DInSAR results from the ascending and descending Sentinel 1A images. Four Sentinel 1A complex data sets, before and after the earthquake, were used between 2022/11/15 and 2020/11/27 for ascending data and 2022/11/14 to 2020/11/26 for descending data. A) and B) Interferogram structures obtained using the ascending and descending data set, C) and D) surface deformations from the ascending and descending dataset. Positive values mean approaching the satellite in the direction of LOS, and negative values mean moving away from the satellite in the direction of LOS. E) Illustration of the east-west deformation. Negative values represent west movement, positive values eastward movement. F) Illustration of vertical deformation. Positive values indicate uplift, negative values indicate subsidence. Active faults are shown with black lines in the Türkiye Active Fault Map (Emre et al., 2013) published by MTA.

A-A' and B-B', shown in Figure 8B, respectively. The cross-sections labeled A-A' and B-B' demonstrate the movement of the LOS in relation to the topography, measured in kilometers. The orange lines represent changes in elevation, while the blue lines indicate displacement, measured in millimeters.

The results of advanced modeling are shown in Figure 9. The forward modeling method was used to return to the result obtained from the ascending data set in Figure 9A. According to this model, approximately 4.53 cm deformation area was determined with the earthquake center to the northwest, keeping the Karadere Segment to the north. The interferogram model corresponding to this area is shown in Figure 9B. The advanced modeling results are shown in Figure 9C for east-west, Figure 9D for vertical, and Figure 9E for north-south components.

## 4. Discussion

According to the DInSAR results for the Gölyaka-Düzce earthquake on November 23, 2022, the ascending data set provides a more consistent result than the descending data set (Figure 5A). The results in the descending data set may have been affected by atmospheric conditions or topography and do not show any surface deformation anomalies from the earthquake center (Figure 5B). Therefore, the results from the ascending data set were evaluated in this study. In Figure 5A, a surface deformation image obtained by unwrapping the interferogram in the

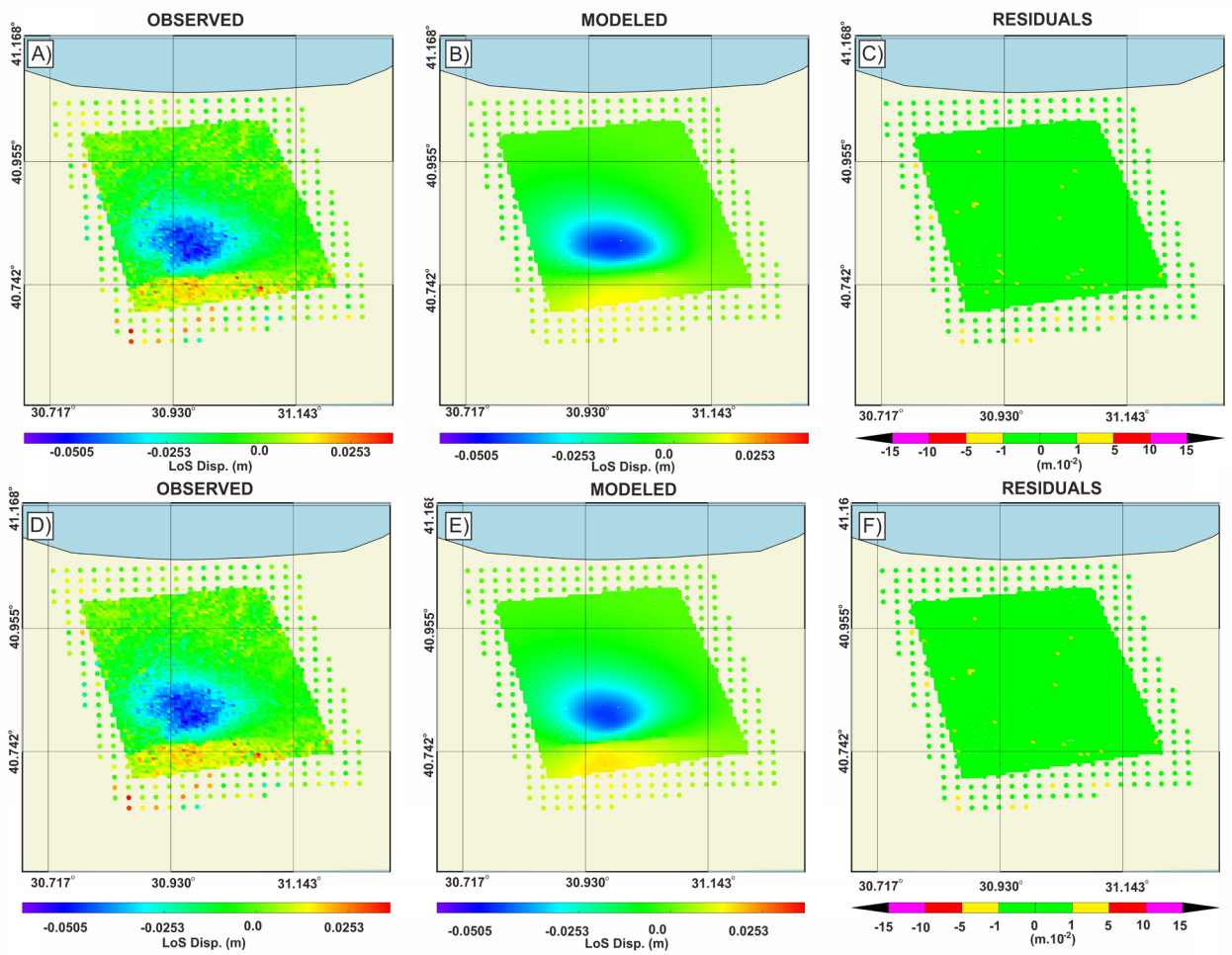


**Figure 6.** Nonlinear inversion: A) The initial observed data, B) The first model was generated based on the observed data, C) The first set of residuals was generated from the shear dislocation with a root mean square (RMS) value of 0.016 m (overall RMS: 0.058 m). Linear inversion: D) corrected observed data, E) generated corrected model, F) the corrected residuals, generated from the shear dislocation, with an RMS value of 0.016 m (overall RMS: 0.055 m).

ascending data set shows movement in an average LOS direction of –6 cm in an area of approximately 100 km$^2$ in the northwest of the Karadere segment (Figure 5C). This movement is interpreted as being right-directional or subsidence in the LOS direction. In addition, the deformation area covers the northwest and southeast blocks of the Karadere segment together, and the deformation boundary in the DInSAR data is located on the Düzce segment. When the deformation boundary on the Düzce segment in the ascending data set is examined, there is movement of an average of 3 cm in a LOS direction in the section south of the Düzce segment, and this situation is interpreted as the westward movement of the southern block of the Düzce fault (Figure 5C). The relative movement of the northern block towards the east and the southern block towards the west, as stated by Yıldırım and Tüysüz (2017) for the Almacık block, is consistent with the DInSAR data. The east-west and vertical components obtained by decomposing the ascending and descending data sets are shown in Figures 5E and 5F. When looking at Figure 5E, the right-lateral strike-slip movement matches the NAF. In Figure 5F, surface deformation with a vertical component is shown, and it is interpreted as subsidence in the northern block and uplift in the southern block of the Düzce segment.

The point sets shown for each iteration step in Monte Carlo analysis were interpreted together and RMS values were obtained from the results in an acceptable manner (Figure 7). There may be relative variability in the consistency of the length and depth values when examined

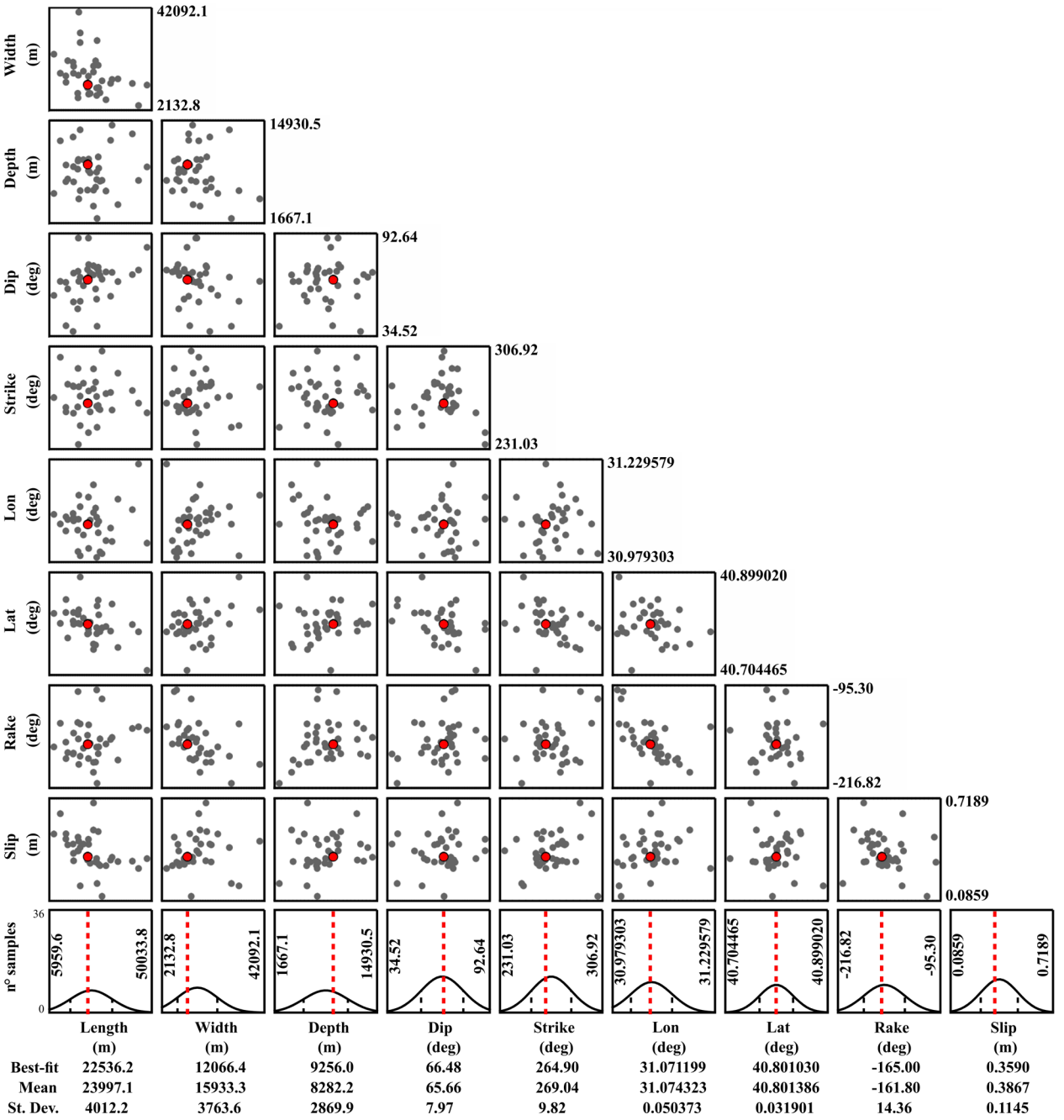


**Figure 7.** Nonlinear inversion statistics showing the uncertainties and changes of the model parameters of the fault that caused the 23 November 2022 Gölyaka-Düzce earthquake using Monte Carlo analysis. Strike, dip, and rake are in degrees; slip is in meters; the X and Y coordinates (representing the center of the fault plane projected upward sloping to the surface) belong to the UTM 36N coordinate system; length, width, and depth in meters. Each of the 50 points in the drawings used for different parameters represents the value for finding the most suitable solution for the selected parameter set.

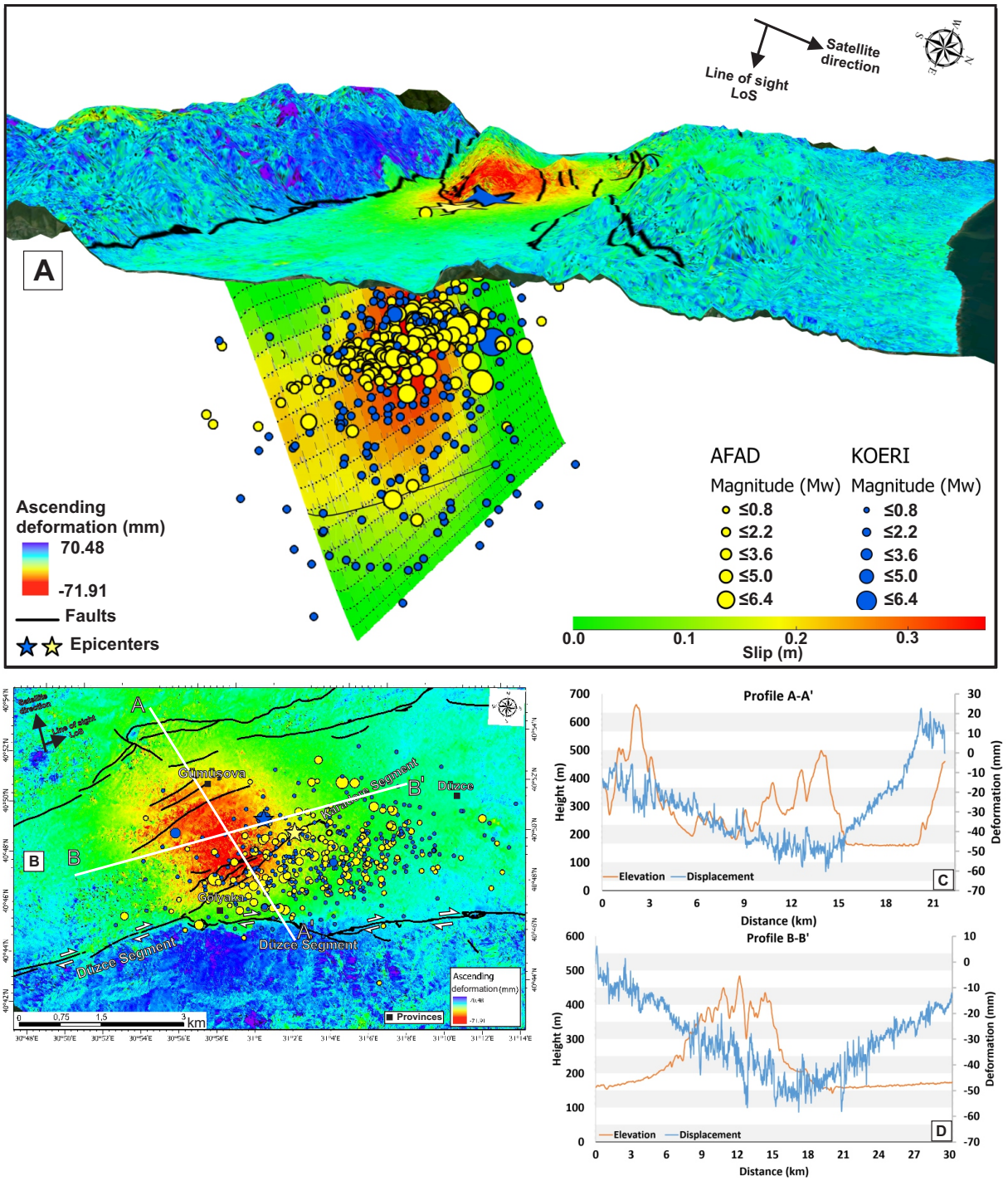


**Figure 8.** A) Ascending data set based on the topography of the 23 November 2022 Gölyaka-Düzce earthquake. The slip model of the earthquake moment and earthquakes in the range of 0.8–6.4 Mw between 22/11/2022 00:01 and 24/11/2022 23:59 are shown. B) The view from the top. Blue dots show earthquake data from KOERI and yellow dots from AFAD. The black lines show the active faults taken from the Active Fault Map of Türkiye (Emre et al., 2013) published by the MTA. Blue star indicates earthquake centers from KOERI and yellow star from AFAD. C) and D) Cross-sections A-A' and B-B' showing LOS motion with topography (in kilometers) respectively. While orange lines show elevation, blue lines indicate the displacement (in millimeters).

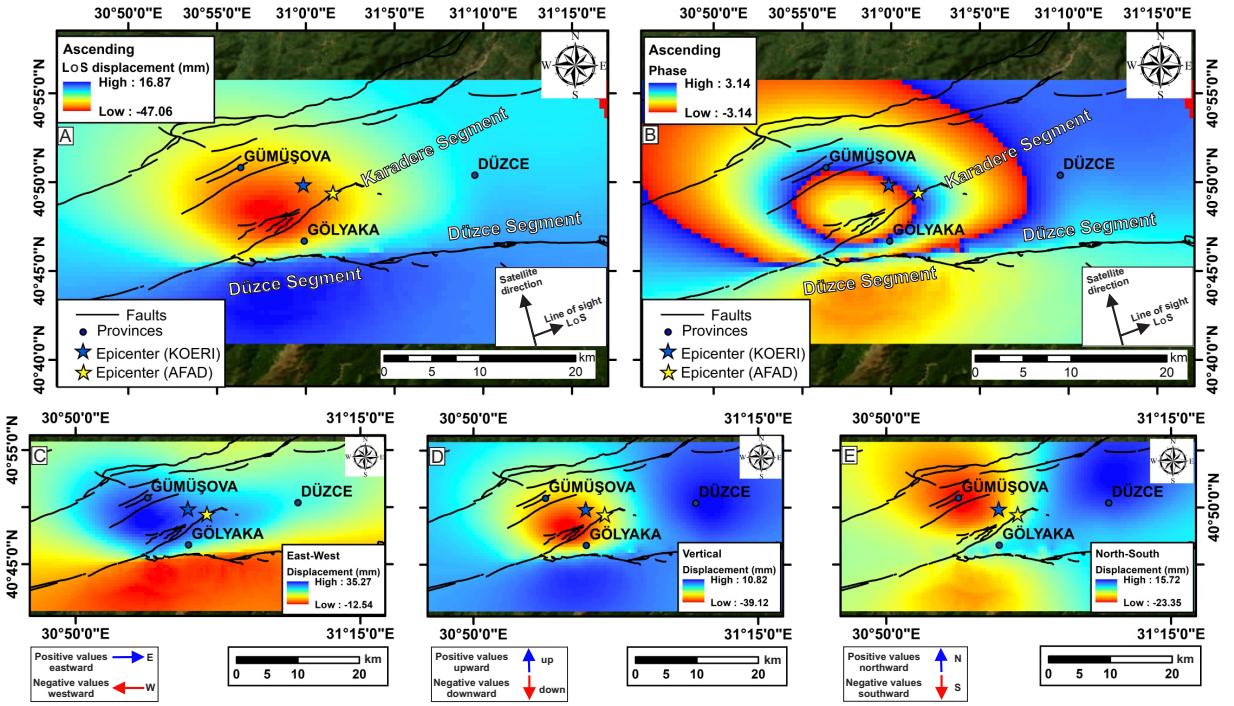


**Figure 9.** Forward modeling; components of displacement produced by the shear distribution obtained through linear inversion: A) Model displacement data, B) Unwrapped interferogram, C) east-west, D) up-down components, E) north-south components (The north-south component accuracy is limited due to the geometrical acquisition of SAR data, with respect to east-west and vertical direction).

for their standard deviations, although the best-fit values obtained for strike, dip, and rake through Monte Carlo analysis are in consistent agreement with earthquake research centers (Figure 7). In addition, it is compatible with the results of the Moment Tensor analysis (Table 2).

In Figure 8A, a north-dipping fault plane on the Düzce segment with maximum slip approximately 0.35 m is shown at a slip-centroid depth of about 9.2 km, which was obtained with the elastic dislocation result from the ascending data set. The earthquakes taken from AFAD and KOERI earthquake catalogs are located in the northern block of the Düzce segment (Figure 8B) and these earthquakes appear in both the northern and southern blocks of the Karadere segment. Therefore, the main earthquake is considered to have actually affected the Düzce segment, and the Karadere segment was affected by this earthquake. In addition, the structure of the north-dipping fault plane obtained as a result of elastic modeling matches the earthquakes before and after this earthquake, and that earthquakes in the western region may be independent of the Karadere segment.

In earthquake focal mechanism solutions obtained from some institutions, the strike values range from 255 to 264, the dip values range from 63 to 77, and the rake values range from –152 to –175. The focal mechanism solution of AFAD has a strike value that falls outside this range. However, the dip and rake values are consistent with the values in this study and from other focal solutions. Additionally, if we consider that the north-dipping fault has a depth of approximately 9 to 17 km, the dip direction and earthquake locations appear to be consistent (Figure 5C). The crucial aspect to consider is the dip direction of the Karadere segment. Focal mechanism solutions obtained from other institutions except for AFAD, GFZ, and DEU-DAUM show a north-dipping solution according to tensor solutions. These north-dipping solutions are consistent with the Düzce segment.

In this study, the modeling results show the dip angle of around 66 degrees to the north. The dip angle difference between Emre et al. (2013) and our work can be interpreted as follows; if the depth of the earthquake is considered to be 6–19 km, the 66 degree dip is reasonable due to the possibility of not determining the real angle of the fault between 6 and 19 km depth. Moreover, dip angle results for the earthquake from observation stations are shown in Table 2. Most of the observation stations provide a dip angle of 60–80 degrees, which is compatible with the results of this study.

**Table 2.** The 2022 Düzce-Gölyaka earthquake information received from the United States Geological Survey Comprehensive Earthquake Catalog (USGS[5]), the GCMT[6] , the AFAD[1], KOERI[2], the Institut de Physique du Globe de Paris (IPGP[7]), GéoAzur, Université de Nice Sophia-Antipolis, Valbonne (OCA[8]), GeoForschungsZentrum Postdam (GFZ[9]). While bold black numbers are related to fault parameters of the relevant actual fault plane caused by the earthquake, others show auxiliary plane fault parameters.

| | | *Depth (km)* | *Magnitude (Mw)* | *Lat.* | *Lon.* | *Plane 1* | | | *Plane 2* | | |
|---|---|---|---|---|---|---|---|---|---|---|---|
| | | | | | | Strike | Dip | Rake | Strike | Dip | Rake |
| *USGS*[3] | | 18 | 6.1 | 40.836° | 30.983° | 160 | 63 | –19 | **259** | **73** | **–152** |
| *GCMT*[4] | | 14.6 | 6.1 | 40.870° | 31.060° | **257** | **77** | **–175** | 166 | 85 | –13 |
| *KOERI*[2] | | 10 | 6 | 40.83° | 31.0° | 167 | 88 | –16 | **257** | **73** | **–178** |
| *AFAD*[1] | | 6.81 | 5.9 | 40.823° | 31.025° | **77** | **65** | **–168** | 342 | 79 | –26 |
| *IPGP*[5] | | 12 | 6.1 | 40.844° | 30.969° | **257** | **72** | - | 165 | 82 | - |
| *OCA*[6] | | 11 | 6.1 | 40.82° | 30.99° | **255** | **60** | **–176** | 163 | 86 | –30 |
| *GFZ*[7] | | 19 | 6.1 | 40.80° | 31.08° | 345 | 80 | –16 | **78** | **74** | **–169** |
| ***This Study*** | **Focal Mech.** | 14 | 5.9 | 40.82° | 30.99° | 165 | 85 | –20 | **257** | **70** | **–175** |
| | **Modeling** | 9.2 | 6.1 | 40.80° | 31. 07° | **264** | **66** | **–165** | - | - | - |

High correlation was detected between the results obtained from forward modeling and DInSAR data (Figures 5A, 8A, and 8B). When examined in detail, the two repeated structures in the unwrapped results in Figure 5A were also similar to those obtained in forward modeling in Figure 9B. Similarly, high similarity was observed between the surface deformation ratio and horizontal and vertical components observed in Figure 5C and the values modeled in Figure 9A. The surface deformation boundaries in forward modeling results are also located on the Düzce segment.

## 5. Conclusions

In this study, surface deformations that occurred after the Gölyaka-Düzce earthquake on November 23, 2022, were determined using the DInSAR method. Four sets of Sentinel 1A complex (SLC-Single Look Complex) data were used, including two ascending and two descending pre- and postearthquake data sets dated November 15, 2022, November 27, 2020, November 14, 2022, and November 26, 2020. Both east-west and vertical surface deformation movements were calculated by separating the components of these two data sets. Additionally, linear and

4 EMSC (2022). European-Mediterranean Seismological Centre [Online]. Website: https://static2.emsc.eu/Images/EVID/119/1191/1191966/1191966.MT.jpg [accessed 2023/01/11].

5 USGS (2022). United States Geological Survey [Online]. Website: https://earthquake.usgs.gov/earthquakes/eventpage/us7000irp8/executive [accessed 2023/01/11].

6 GCMT (2022). Global Centroid Moment Tensor [Online]. Website: https://www.globalcmt.org/CMTsearch.html [accessed 2023/01/11].

7 IPGP (2022). Observatoire GEOSCOPE Institut de physique du Globe de Paris [Online]. Website: http://geoscope.ipgp.fr/index.php/en/catalog/earthquake-description?seis=us7000irp8 [accessed 2023/01/11].

8 Oca 6 OCA (2022). GéoAzur, Université de Nice Sophia-Antipolis, Valbonne, France [Online]. Website: https://sismoazur.oca.eu/#/focal mechanism/emsc [accessed 2023/01/11].

9 GFZ (2022). GeoForschungsZentrum Postdam, Germany [Online]. Website: http://geofon.gfz-potsdam.de/eqinfo/event.php?id=gfz2022wxsg [accessed 2023/01/11].

nonlinear inversion were applied to determine the amount of fault slip and the distribution of fault surface slip for the fault using data obtained from DInSAR results and the Global Centroid Moment Tensor catalog, and elastic dislocation modeling was performed.

The results of DInSAR, elastic dislocation modeling, and tensor analysis for the Gölyaka-Düzce earthquake on November 23, 2022, are as follows:

Based on the DInSAR findings, the deformation occurred in the northwestern part of the Karadere segment. Covering an area of around 105 $km^2$, this deformation consists of both eastward movement and subsidence. The eastward movement is compatible with the tectonic structure of the Düzce segment on the right-lateral North Anatolian Fault.

During the earthquake, there was an observed eastward and downward displacement of approximately 0.35 m at a slip-centroid depth of around 9.2 km. The deformation boundaries indicate that this displacement occurred in the Düzce segment of the fault. This is compatible with the clockwise movement of the northern branch of the Almacık block (Yıldırım and Tüysüz, 2017). The tensor solutions obtained from earthquake centers other than AFAD, GFZ, and DEUM, as well as the tensor solution from this study revealed a north-dipping orientation with an approximate east-west direction. This orientation aligns with the geometry of the Düzce segment.

The aftershocks that occurred both before and after the earthquake, covering both the northern and southern blocks of the Karadere segment and clustering on the northern block of the Düzce segment, support the idea that the main earthquake occurred on the Düzce segment.

According to the results of DInSAR, elastic modeling, and tensor analysis, on November 23, 2022, the Gölyaka-Düzce earthquake caused both right-lateral and descending motion in the northwest part of the Karadere segment. The boundary of this deformation motion is believed to be the Düzce segment and includes the Karadere segment. Also, the locations of the aftershocks and foreshocks in the northern part of the Düzce segment support the idea that the main earthquake occurred on the Düzce segment. However, it is also thought that this earthquake affected the Karadere segment.

**Data availability**

Sentinel-1 data are available online through Copernicus (https://scihub.copernicus.eu) platforms. Precise orbits were downloaded from European Space Agency's Sentinel1 website (https://qc.sentinel1.eo.esa.int/, in December 2022). SRTM data were provided on the Earthdata portal (https://earthdata.nasa.gov).

**Acknowledgment**

This study was supported by the General Directorate of Mineral Research and Exploration (MTA). We thank Prof. Dr. Semih Ergintav, Prof. Dr. Bülent Kaypak, Dr. Akın Kürçer, and Hasan Elmacı for their help with discussions on various aspects of this research. The authors would also like to special thank Simone Atzori and Prof. Dr. Derman Dondurur for their insightful constructive comments and suggestions. Thanks are extended to the European Space Agency for giving free access to the Sentinel-1 data through the Copernicus Hub.

**Author contributions**

Ş. O. Karaca: Conceptualization, original draft preparation, dataset collection, InSAR data analysis, elastic dislocation modeling process, methodology, validation, manuscript writing, review, and editing. G. Erten: Elastic dislocation modeling process, manuscript writing, review, and editing. B. Yıkmaz: Moment Tensor Analysis process. S. Özalp: Tectonic model.

Regarding the interpretation presented in this paper, the author (S.Ö.) holds a different perspective. Specifically, he disagrees with identifying the source fault of the 23 November 2022 Gölyaka (Düzce) Earthquake as the Düzce Segment. Instead, he argues that the Karadere Segment serves as the source fault for the recent earthquake. His detailed discussion of this interpretation is presented elsewhere (Özalp et al., 2023).

**Conflicts of interest**

The authors declare no conflict of interest.

## References


Abdikan S, Imamoglu M, Alasag T, Toker M, Kutoglu SH et al. (2019). Insar analysis of Ayvacik 2017 (mw 5.3) earthquake swarm (Canakkale, NW-Turkey). International Archives of the Photogrammetry, Remote Sensing and Spatial Information Sciences 2/W13: 1907–1911. https://doi.org/10.5194/isprs-archives-XLII-2-W13-1907-2019

AFAD (2022). Türkiye Cumhuriyeti İçişleri Bakanlığı Afet ve Acil Durum Yönetimi Başkanlığı, Deprem ve Risk Azaltma Genel Müdürlüğü, 23 Kasım 2022 Gölyaka (Düzce) mw 5.9 depremine ilişkin ön değerlendirme raporu (in Turkish).

Aktuğ B (2003). Elastik yarı uzay modelleri ve depremsel koordinat değişimlerine dinamik bir yaklaşım. Harita Dergisi 70 (129): 1 – 16 (in Turkish).

Aşcı M, Yas T (2017). Doğal kaynaklı potansiyel alanların birleşik ters çözümü. Uygulamalı Yerbilimleri Dergisi 16 (1): 27-50 (in Turkish).

Bamler R, Hartl P (1998). Synthetic aperture radar interferometry. In inverse problems 14 (4): 1-54 https://dx.doi.org/10.1088/0266-5611/14/4/001

Başokur AT (2015). Türev tabanlı parametre kestirim yöntemleri. Türk Mühendis ve Mimar Odaları Birliği, Jeofizik Mühendisleri Odası yayını No:22, Ankara (in Turkish).

Çakır Z, Barka A, Akyüz S (2003a). Coulomb gerilme etkileşimleri ve 1999 Marmara depremleri. İstanbul Teknik Üniversitesi Dergisi Mühendislik 2 (4): 99-111 (in Turkish).

Çakır Z, Barka AA, De Chabalier J, Armijo R, Meyer B (2003b). Kinematics of the November 12, 1999 (Mw=7.2) Düzce earthquake deduced from SAR interferometry. Turkish Journal of Earth Sciences 12 (2003): 105-118.

Emre Ö, Duman TY, Özalp S, Elmacı H, Olgun Ş et al. (2013). Açıklamalı Türkiye diri fay haritası. Ölçek 1:1.250.000, Maden Tetkik ve Arama Genel Müdürlüğü, özel yayın serisi-30, Ankara-Türkiye (in Turkish).

Funning GJ, Parsons B, Wright TJ, Jackson JA, Fielding EJ (2005). Surface displacements and source parameters of the 2003 Bam (Iran) earthquake from Envisat advanced synthetic aperture radar imagery. Journal of Geophysical Research: Solid Earth. 110 (9): 1–23. https://doi.org/10.1029/2004JB003338

Ganas A, Kourkouli P, Briole P, Moshou A, Elias P et al. (2018). Coseismic displacements from moderate-size earthquakes mapped by Sentinel-1 differential interferometry: The case of February 2017 Gulpinar earthquake sequence (Biga Peninsula, Turkey). Remote Sensing 10 (7): 1089. https://doi.org/10.3390/rs10071089

Ganas A, Elias P, Briole P, Valkaniotis S, Escartin J et al. (2021). Co-seismic and post-seismic deformation, field observations and fault model of the 30 October 2020 Mw = 7.0 Samos earthquake, Aegean Sea. Acta Geophysica 69 (3): 999–1024. https://doi.org/10.1007/s11600-021-00599-1

Gedik İ, Aksay A (2002) 1:100000 Ölçekli Türkiye jeoloji haritaları, Adapazarı-G25 paftası No:32. Maden Tetkik ve Arama Genel Müdürlüğü, Jeoloji Etütleri Dairesi, Ankara (in Turkish).

Helz RL (2005). Monitoring ground deformation from space. United States Department of the Interior, United States Geological Survey.

Jost ML, Herrmann RB (1989). A student's guide to and review of moment tensors. In Seismological Research Letters 60 (2): 37–57. https://doi.org/10.1785/gssrl.60.2.37

Karaca ŞO, Erten G (2023). DInSAR and Elastic Dislocation Modelling: A case study for the 24 January 2020 Elazig-Sivrice earthquake. Turkish Journal of Remote Sensing 5 (1): 1-13. https://doi.org/10.51489/tuzal.1187819

Kotulak N, Mleczko M, Crosetto M, Palamà R, Mróz M (2022). Interferometric SAR deformation monitoring using passive reflectors and ascending and descending passes. International Archives of the Photogrammetry, Remote Sensing and Spatial Information Sciences 43 (B3-2022): 285–292. https://doi.org/10.5194/isprs-archives-XLIII-B3-2022-285-2022

Liu Y (2015). InSAR technique for earthquake studies, MSc. Geoscience and Earth Observing Systems Group, School of Civil and Environmental Engineering Faculty of Engineering, The University of New South Wales. https://doi.org/10.26190/unsworks/18850

Marquardt DW (1963). An algorithm for least-squares estimation of nonlinear parameters. Journal of the Society for Industrial and Applied Mathematics 11 (2): 431–441. https://doi.org/10.1137/0111030

Melgar D, Ganas A, Taymaz T, Valkaniotis S, Crowell B et al. (2020). Rupture kinematics of 2020 January 24 Mw 6.7 Doğanyol-Sivrice, Turkey earthquake on the East Anatolian Fault Zone imaged by space geodesy, Geophysical Journal International 223 (2): 862–874, https://doi.org/10.1093/gji/ggaa345

Okada Y (1985). Surface deformation due to shear and tensile faults in a half-space. Bulletin of the Seismological Society of America 75 (4): 1135-1154. https://doi.org/10.1785/BSSA0750041135

Özalp S, Kürçer A, Avcu İ, Güler T (2023). 23 Kasım 2022 Gölyaka (Düzce) depremi (mw 6,0) arazi gözlemleri ve kaynak faya ilişkin değerlendirmeler. Maden Tetkik ve Arama Genel Müdürlüğü, Yerbilimleri ve Madencilik Dergisi 3 (3): 61-80 (in Turkish).

Parsons B, Wright T, Rowe P, Andrews J, Jackson J et al. (2006). The 1994 Sefidabeh (eastern Iran) earthquakes revisited: new evidence from satellite radar interferometry and carbonate dating about the growth of an active fold above a blind thrust fault. Geophysical Journal International 164 (1): 202–217. https://doi.org/10.1111/j.1365-246X.2005.02655.x

Pousse Beltran L, Nissen E, Bergman EA, Cambaz MD, Gaudreau É et al. (2020). The 2020 Mw 6.8 Elazığ (Turkey) earthquake reveals rupture behavior of the East Anatolian Fault. Geophysical Research Letters 47 (13). https://doi.org/10.1029/2020GL088136

Press F (1965). Displacements, strains, and tilts at teleseismic distance. Journal of Geophysical Research 70 (10): 2395-2412. https://doi.org/10.1029/JZ070i010p02395

Sarychikhina O, Glowacka E (2015). Spatio-temporal evolution of aseismic ground deformation in the Mexicali Valley (Baja California, Mexico) from 1993 to 2010, using differential SAR interferometry. Proceedings of the International Association of Hydrological Sciences 372: 335–341. https://doi.org/10.5194/piahs-372-335-2015

Sözbilir H, Utku M, Ankaya O, Çırmık A, Özdağ ÖC et al. (2023). 23 Kasım 2022 Mw5.9 Gölyaka-Düzce depremi ön gözlem ve değerlendirme raporu. Dokuz Eylül Üniversitesi, Deprem Araştırma ve Uygulama Merkezi, İzmir, Türkiye (in Turkish).

Stein S, Wysession M (2003). An introduction to seismology, earthquakes, and earth structure. Geological Magazine 140 (6): 727-735. https://doi.org/10.1017/S0016756803318837

Stekeete JA (1958). On Volterra's dislocations in a semi-infinite elastic medium. Canadian Journal of Physics 36 (2): 192-205. https://doi.org/10.1139/p58-024

Tatar O, Sözbilir H, Koçbulut F, Bozkurt E, Aksoy E et al. (2020). Surface deformations of 24 January 2020 Sivrice (Elazığ)–Doğanyol (Malatya) earthquake (mw = 6.8) along the Pütürge segment of the East Anatolian Fault Zone and its comparison with Turkey's 100-year-surface ruptures. Mediterranean Geoscience Reviews 2 (3): 385–410. https://doi.org/10.1007/s42990-020-00037-2

Tiryakioğlu İ, Aktuğ B, Yiğit C, Yavaşoğlu HH, Sozbilir H et al. (2018). Slip distribution and source parameters of the 20 July 2017 Bodrum-Kos earthquake (Mw6.6) from GPS observations. Geodinamica Acta 30 (1): 1–14. https://doi.org/10.1080/09853111.2017.1408264

Torres R, Snoeij P, Geudtner D, Bibby D, Davidson M et al. (2012). The global monitoring for environment and security, Sentinel-1 mission. Remote Sensing of Environment 120: 9–24. https://doi.org/10.1016/j.rse.2011.05.028

Vavryčuk V (2015). Moment tensors: decomposition and visualization. In Encyclopedia of Earthquake Engineering 1–16. https://doi.org/10.1007/978-3-642-36197-5_288-1

Yague Martinez N, Prats Iraola P, Gonzalez FR, Brcic R, Shau R et al. (2016). Interferometric processing of Sentinel-1 TOPS data. Institute of Electrical and Electronics Engineers, Transactions on Geoscience and Remote Sensing 54 (4): 2220–2234. https://doi.org/10.1109/TGRS.2015.2497902

Yıldırım C, Tüysüz O (2017). Estimation of the long-term slip, surface uplift and block rotation along the northern strand of the North Anatolian Fault zone: inferences from geomorphology of the Almacık Block. Geomorphology 297: 55–68. https://doi.org/10.1016/j.geomorph.2017.08.038

Wang R, Xia Y, Grosser H, Wetzel HU, Kaufmann H et al. (2004). The 2003 Bam (SE Iran) earthquake: precise source parameters from satellite radar interferometry. Geophysical Journal International 159 (3): 917–922. https://doi.org/10.1111/j.1365-246X.2004.02476.x

Wells DL, Coppersmith KJ (1994). New empirical relationships among magnitude, rupture length, rupture width, rupture area, and surface displacement. In Bulletin of the Seismological Society of America 84 (4): 974–1002. https://doi.org/10.1785/BSSA0840040974

Welstead ST (1999). Fractal and wavelet image compression techniques. Society of Photographic Instrumentation Engineers Optical Engineering Press, Bellingham, Washington, 232. https://doi.org/10.1117/3.353798

Wright TJ, Parsons BE, Jackson JA, Haynes M, Fielding EJ et al. (1999). Source parameters of the 1 October 1995 Dinar (Turkey) earthquake from SAR interferometry and seismic bodywave modelling. In Earth and Planetary Science Letters 172 (1-2): 23-37 https://doi.org/10.1016/S0012-821X(99)00186-7

Zebker HA, Goldstein RM (1986). Topographic mapping from interferometry synthetic aperture radar observations. Journal of Geophysical Research 91 (B5): 4993–4999 http://dx.doi.org/10.1029/JB091iB05p04993